A Digital Blueprint for 3D-Printing Lab Scale Aqueous and Organic Redox-Flow Batteries

Luuk Kortekaas+,[a] Sebastian Fricke+,[a] Aleksandr Korshunov,[b] Martin Winter,[a, b] Isidora Cekic-Laskovic,*[a] and Mariano Grünebaum*[a]

As 3D-printing is becoming increasingly accessible, its application towards more sustainable and flexible design strategies for chemical processes also grows substantially. Redox-flow batteries (RFBs) are recognized as one of the possible next generation energy storage solutions, owing to the inherent decoupling of power and energy, yet the capital costs involved produce a high barrier to enter the field. Here, we demonstrate a full digital blueprint for printing one's own RFB, that can enable more (organic chemistry) contributions to the field. At the time of writing, the combined costs of only the RFB cell total around 60 €, which is less than commercially available RFB cells by a great margin. The cyclic voltammetry, impedance spectroscopy and potentiostatic cycling experiments exemplified by the $K_4[Fe^{II}(CN)_6]\,|\,K_3[Fe^{III}(CN)_6]$ redox-pair for aqueous, and ferrocene | ferrocenium for organic electrolytes, validate the stability of the technical lab-scale design and provides benchmark values for reproduction.

Introduction

Over the last decades, the ever-growing demand for renewable energy has turned energy storage into a vital research area. Generally, batteries are recognized as a most excellent storage solution, offering flexibility in not only their engineering, but also their chemical make-up, ultimately providing tuneable durability and capacity.[1] Redox-flow, in particular, offers a large playground for a synthetic chemist, as the capacity and voltage are directly linked to the solubility (of charged states), number of electrons passed, and separation of redox-events.[2,3] Although the synthetic chemist's toolbox is ever expanding and constantly reaching new heights,[3–5] not all organic chemistry-oriented groups possess the engineering know-how to put their chemical expertise to the test, and commercially available redox-flow batteries (RFBs) require a high capital investment. Notably, the costs of the cell and pump are

considered only in detailed cost analyses due to a general lack of alternative options.[6]

A rapidly growing alternative to expensive commercially available resources is additive manufacturing, or 3D-printing.[7–9] 3D-printing consists of a range of techniques, that have found solid footing already in peristaltic pumps[10,11] flow reactors cells[12] and (components of) batteries,[13–15] such as laser sintering/melting (LS) and fused deposition modelling (FDM) for constructing 3D (metallic) electrodes[16–18] and masked stereolithography (MSLA) for cell components.[15,16] Classically, injection moulding and milling are also suitable for creating cell assemblies. The machining of a polymer sheet cut out the desired cavities is, however, a slow and costly procedure with a resolution limited to the quality of the milling machine.[18,19] Injection moulding, on the other hand, is a low-cost technique and enables mass production at a quicker rate even than 3D-printing,[8] but the frequent redesigning in prototypical flow-cells and the need for only a several cells at lab-scale make injection moulding prohibitively expensive.[14] In fact, the high degree of design freedom in MSLA 3D-printing, specifically, allows for continuous and rapid adjustments at nowadays impressively high resolution (we use a 300 € Elegoo Mars 3 Pro printer with a 35 μm XY-resolution), showing promise for substantially cutting costs as well as increasing quality of components. Further notable advances in the field of 3D-printing include the increasing number of commercially available resins, improving their chemical as well as mechanical resistance, making it feasible to 3D-print the entire casing as well.[7] And although a stainless steel casing for a 3D-printed RFB proved to be efficient in housing the modular 3D-printed flow cell components,[14] the inclusion of the casing in the design allows for yet more flexibility and cutting down of costs.[8] Similarly, whilst our current contribution was in the making, O'Connor et al. reported an open-source 3D-printable cell stack, reducing production costs of an RFB cell to ∼99 €

[a] Dr. L. Kortekaas,+ S. Fricke,+ Prof. Dr. M. Winter, Dr. I. Cekic-Laskovic, Dr. M. Grünebaum
Helmholtz Institute Münster, IEK-12,
Forschungszentrum Jülich GmbH
Corrensstrasse 46, 48149 Münster (Germany)
E-mail: i.cekic-laskovic@fz-juelich.de
m.gruenebaum@fz-juelich.de
[b] A. Korshunov, Prof. Dr. M. Winter
MEET Battery Research Center
University of Münster
Corrensstrasse 46, 48149 Münster (Germany)
[+] These authors contributed equally to this work.

compared to ~ 2,300–4,000 € commercially available alternatives.[20] Although the brass current collector endplates in the RFB stack serve as their own encasing, printing them with resin instead improves the scalability and reduces processing costs of the cell.

Here, we developed a procedure to construct full cell enclosed RFBs through 3D-printing that includes a 3D-printed peristaltic pump. The complete RFB (54.60 €), including peristaltic pump (135.23 €) and glove bag (38.30 €), uses only small, inexpensive components, with a net worth totalling ≈ 230 € at the time of writing (Table S1). This leaves only the electrolyte solution and the membrane or separator, which needs to be selected individually based on the electrolyte (for reference, ca. 14 cm^2 of separator or membrane per RFB are needed).

The design itself comprises of a typical stack of current collector, electrode, rubber sealing and membrane, using inexpensive graphite and porous carbon felt.[8] The 3D-structure of the conductive carbon felt additionally provides an increased contact surface area for the electrolyte that flows directly through. It is advised to bear in mind that computational studies can aid in finding the right flow rate and internal cell pressure for a system, as both can be adjusted.[21,22] The highly affordable lab-scale setup (versus commercial lab-scale systems) thus allows for a widely accessible initial screening of an electrolyte's, e.g., open circuit potential, power density, energy efficiency and charge-discharge behavior.[8,23] Furthermore, we note that although the current scale is already suitable for a throughput of 1 mL s^{-1} (mean linear flow velocity $\nu =$ 0.42 cm s^{-1};[14] Figure 2, right), rescaling of all components, printable and commercial (e.g., graphite electrodes, tubing and bearing size), is theoretically possible by adapting the 3D-file and cutting out differently sized membranes, silicone rubbers, electrodes etc.,[19] allowing also for continuing adjustments in power output.[22] The use of a high-resolution MSLA 3D-printer also affords more precise designs compared to FDM processes (see also, e.g., the flow distributors in our cells[4,8,14]), theoretically enabling even scale-down to mini-cell assemblies when desired. It should be noted, however, that scaling chemical reactors up or down creates additional challenges in mass transport and pressure drops that thus require further optimization.[8,24,25] Such inhomogeneity in reaction conversion over the active electrode area can lead to parasitic reactions, and although mass transfer issues are to some extent reduced in the zero-gap electrode architecture that is used here also, global mass transfer is essential when considering rescaling.[24]

An additional advantage of 3D printing, next to the practicality of easily rescaling components, is the minimization of waste produced and transport. MSLA 3D printing, specifically, produces the input model directly and with little waste, thus limiting the environmental impact primarily to the resin used.[26] Repairs can also be carried out in-house, as described in the Troubleshooting Section of the Supporting Information, so that costly and environmentally unfriendly transport processes to the manufacturer can be avoided. Furthermore, with most resins used, broken components can simply be disposed of in household waste after chemical decontamination.
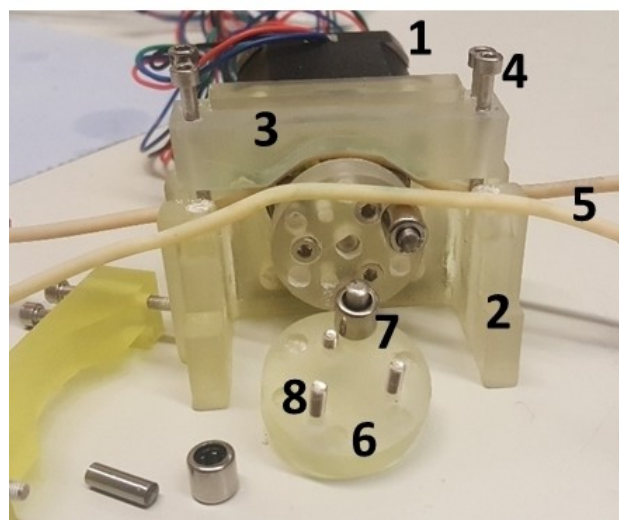
Ultimately, with the design presented here, we show that a dataset with the well-known ferrocene│ferrocenium redox-pair (organic redox-flow; Fc and FcBF$_4$, respectively) as well as K$_4$[Fe^{II}(CN)$_6$]/K$_3$[Fe^{III}(CN)$_6$], (aqueous redox-flow) not only highlights the specifications of the home-built lab-scale RFB, but as benchmark values with a standard redox system also further contributes to enabling replication for lab-scale battery testing elsewhere.
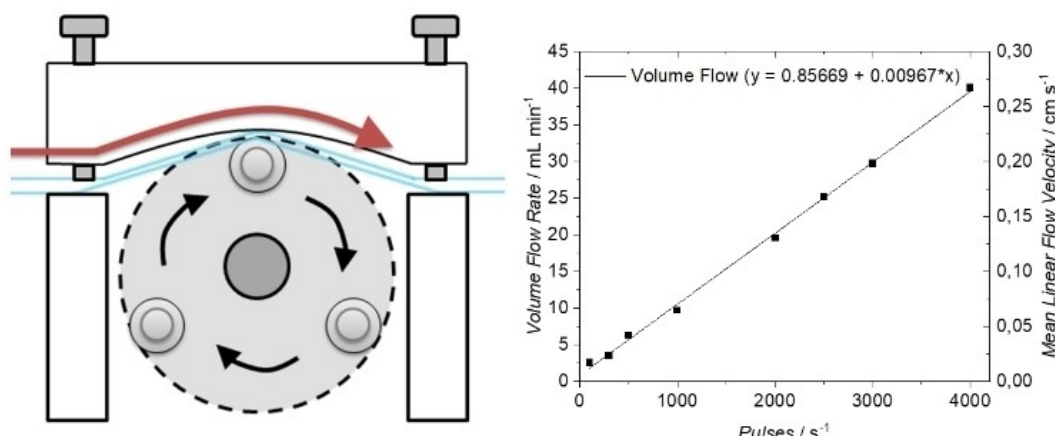
Results and Discussion

Pump design

Owing to its design flexibility and ease of application a peristaltic pump was favoured for the 3D-printable RFB.[10,11] In terms of electrical components, this requires a stepper motor, a stepper motor controller and a power block (Figure S1). Basic design principles for realizing peristaltic motion through 3D-printed utilities were taken from the open access source from the University of Aachen,[27] adaptations most notably include the addition of a second head to facilitate both anolyte and catholyte flow with a single pump (Figure 1).

All 3D-printed components have been optimized for the current scale of the RFB, but scaling components can allow for scaling of the system, bearing in mind re-optimization may be needed to account for, e.g., new potential- and current-distributions, uniformity of mass transport and pressure-drops.[8,24,25] We note that the shrinkage specific to the applied resin could cause minor misfits. Dimensions are standardized, however, and thus the components are suitable for post-processing with appropriate drill bits or thread cutters (see

Figure 1. Front end of the peristaltic pump with 3D-printed components, showing several parts of the front motor head in a disassembled state. (1) Stepper motor. (2) Stepper motor holder. (3) Motor head top bar. (4) 25 mm M3 screws for tightening the bars (back pair) and pinning down the tubing (front pair). (5) Pharmed BPT tubing, outer diameter 3,22 mm, inner diameter 1,52 mm. (6) Motor head block. (7) Rod and bearing (3× for each motor head). (8) 16 mm M3 Screws to connect the motor heads (3× each).
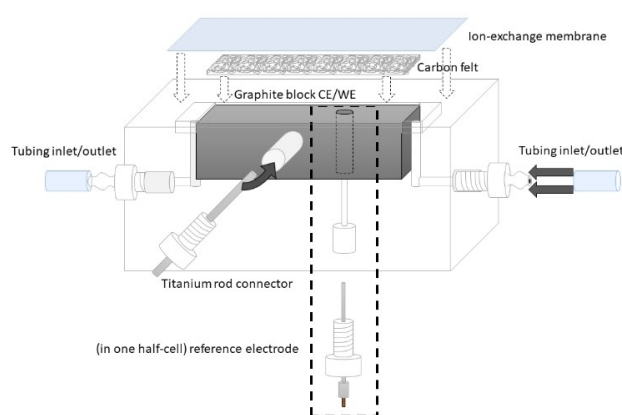
Figure 2. (Left) Schematic of the peristaltic motion realised by the motor block design. (Right) Calibration of the flow rate of the RFB. Monitoring the volume change of acetonitrile over time, transferring acetonitrile from one tank to another at varying stepper motor pulses per second, yields a calibration curve for flow rate for each respective half-cell. Linear regression provides the volumetric flow rate and mean linear flow velocity at varying pulses per second.

"Work-up for the 3D-printed components" in the Supporting Information). As seen in Figure 1, the stepper motor (1) is housed by the motor block holder (2), fastened in place with screws to keep the motor from tilting upon applying force on the top bars (3) through peristaltic motion. The back set of screws (4) in the top bar serves as attachment to the motor block holder (2), the front set serving to pin down the silicon tubing (5) just enough to prevent it from moving during peristaltic motion. The motor head blocks (6) sandwich bars with bearings (7) in between them, compressed with screws. Ultimately, the peristaltic motion succeeds through the bearings (7) unidirectionally pushing up the tubing (5) against the top bars (3) (Figure 2, left). The direction of rotation determines the direction of flow. For prototyping, Eppendorf vials with septa or glass vials with drilled plastic lids are found to be perfectly suited electrolyte tanks (Figure S2), but of course the electrolyte tanks of RFBs are scalable and can be tailored wherever needed.

The motor is controlled by Pololu© software (Figure S3),[28] in which the motor input can be varied as desired, the pulses per second translating to rotational velocity. Ultimately, the flow rate of the RFB fairly linearly relates to the pulses per second of the peristaltic pump. The exact flow rate is, however, is marginally dependent on the consistency of the flow channels, the alignment of the bearings to the arc of the top bar, and the extent of pinning of the tubing by the screws. A calibration curve should therefore be generated for each RFB, measuring the throughput of acetonitrile at varying pulses per second (Figures 2 and S4), in order to determine the exact output during the final battery operation. By using carbon felt electrodes with enhanced 3-dimensional surface area, relatively lower mean linear flow velocities are required for similar electrolyte conversion compared to fixed flow field designs ($v = 1$–$10\ \mathrm{cm\,s^{-1}}$).[14,29]

Cell design

For ease of use, a zero-gap "flow through" configuration in plane parallel flow channels was opted for in the redox-flow cell, with carbon felt as the prime active electrode.[8,19,30,31] The cell can be divided up in two half-cells separated by a membrane or separator (in our case Nafion® N551Na for aqueous cell testing and a Celgard® 2500 for organic; Figures 3 and S5C). We note that membranes are critical to RFB performance and thus hold high importance in getting the overall RFB to function well. A recent review attempted to capture structure-property relationships, providing a possible handle on selecting a membrane that suits the involved electrolytes.[32] As current collector 1.0 by 2.4 cm graphite blocks were selected, topped by carbon felt to increase the contact area, while retaining good conductivity and (electro-)chemical stability.[33] The carbon felt needs to fit neatly in a filed channel in the

Figure 3. Schematic design of a half-cell. A single membrane or separator is the component that separates the two half cells, which are identical except for one having a reference electrode perpendicular to the direction of flow. The titanium rod connectors are wedged into a ca. 2 mm indentation in the graphite blocks, facilitating low-resistance contact (below 10 Ω between the titanium rods when the RFB is loaded with electrolyte and the membrane or separator).

graphite block to ensure low internal cell pressure (Figure S5B), resulting in low risk of cell cracking or leakages. A titanium rod connector facilitates contact with the potentiostat through a 3D-printed screw, with either half- cell serving as cathode or anode. Care has to be taken that the rods are well-inserted into the graphite blocks, so that construction-based potential loss is minimized and potential losses can be attributed solely to the electrolyte or membrane investigated.[31]

Importantly, the half-cell containing the counter electrode (CE) is paired up with a reference electrode (RE, Figure S6), for which a hole is drilled through the graphite block. A channel on either far side of the battery block leads to or from the current collector through tubing hooked up to 3D-printed screws, with the tubing originating from and ending in the fuel tanks, its contents driven by the peristaltic pump (see Figure S2).
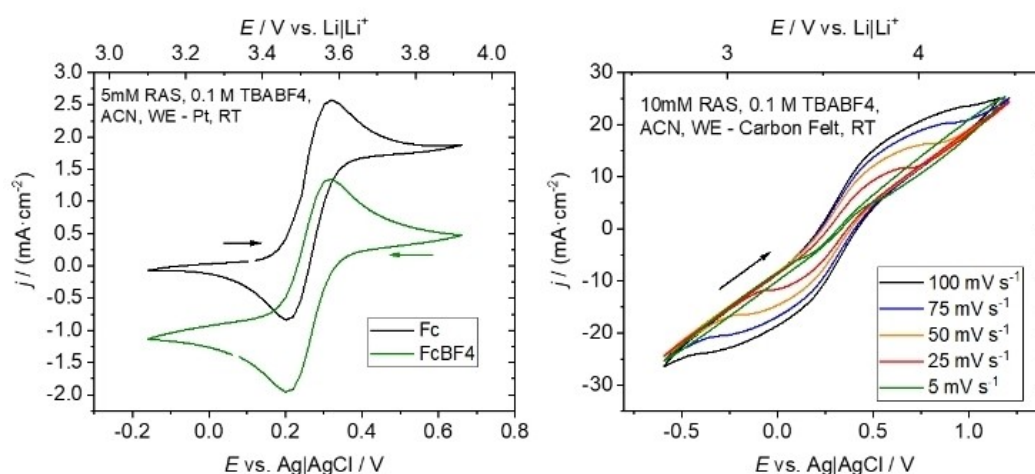
It should be underlined here that a major challenge in designing redox-flow cells is logically related to leakage issues, and although the addition of O-rings and silicone rubbers effectively prevent it,[34] minor assembly flaws can still lead to electrolyte leakage over prolonged periods of time. However, we have included a trouble-shooting section in the Supporting Information, which deals with some reoccurring issues, such as high intercellular pressure leading to material fatigue, broken screws or membrane leakages. Notably, leakages arising from the inner threads of the cell blocks can be avoided by wrapping Teflon tape around the part of the screw threads that will be completely inserted and applying resin to the insertion point after insertion, with subsequent curing by UV-light and curing at elevated temperature to seal the screw in (60 °C over at least 1 night, as shown in Figure S12). Wrapping only Teflon tape around the screw threads initially can ensure a leak-tight performance before setting the screws in more permanently with additional resin. Importantly, this overall design strategy allows for replacing a screw upon breaking of these relative fragile cell components by drilling the former screw out,

instead of having to reprint the cell as a whole, in the case that insertion points were to be directly attached to the battery block. Damaged screws can thus be drilled out with 5 mm drill bit, and the channel re-prepared with an M6 thread cutter (Figure S11).

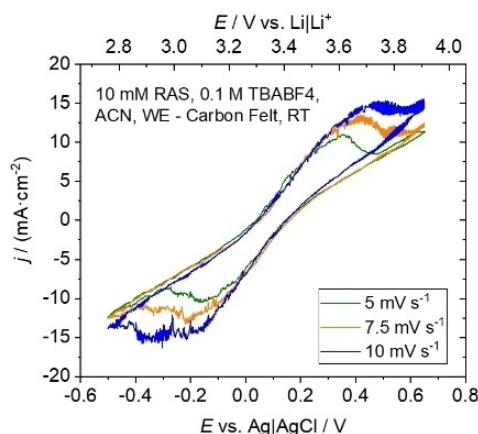### Cyclic voltammetry and impedance spectroscopy evaluation

For prototyping, Armstrong et al. recommended standard redox-pairs Fc/FcBF$_4$ for organic electrolytes (Figure 4 left)[35] and Chen et al. and Lee et al. K$_4$[Fe^{II}(CN)$_6$]|K$_3$[Fe^{III}(CN)$_6$] for aqueous electrolytes (Figure S8 left) were selected, owing to their model electrochemical behaviour, as well as stability in redox-flow.[36,37] As a single redox-event, the electrolytes are naturally not suited for symmetric charge/discharge. However, they do allow us to benchmark the performance of our designed cell, with standard "targets" to aim for when reproducing the redox-flow cells for own use. Electrolyte solutions contain 10 mM Fc or FcBF$_4$, 0.1 M TBABF$_4$ as supporting electrolyte and acetonitrile for the anolyte and catholyte compartment, respectively. For aqueous tests, 50 mM K$_4$[Fe^{II}(CN)$_6$]|K$_3$[Fe^{III}(CN)$_6$] with 1 M KCl as supporting electrolyte in water were used.

When transferring the electrolyte from standard three electrode setup towards static RFB setup a current density increase can be observed, as well as an overall stretching, as described elsewhere (Figure 4 right).[38] The current response of Fc in-flow increases with increasing scan rate as expected. When further applying volume flow (Figures 5 and S9), the peak current increases as expected with higher flow rates, as the rate of refreshing goes up. Note that in the region of mass transport limitation, current noise due to slightly varying convective mass transport from RAS to the three-dimensionally distributed electrode surface (graphite block and carbon felt) causes also variation in current response. These local RAS

Figure 4. Cyclic voltammograms of organic electrolyte in standard CV three electrode setup (left; 5 mM Fc and FcBF$_4$, 0.1 M TBABF$_4$, acetonitrile; 0,3 mL; platinum working electrode, Ag|AgCl reference electrode, stainless steel counter electrode) and static RFB setup (right; 10 mM Fc and FcBF$_4$, 0.1 M TBABF$_4$, acetonitrile; 5 mL; graphite felt and block working electrode and counter electrode, Ag|AgCl reference electrode, Celgard® 2500 separator) at 50 mV s^{-1} scan rate.
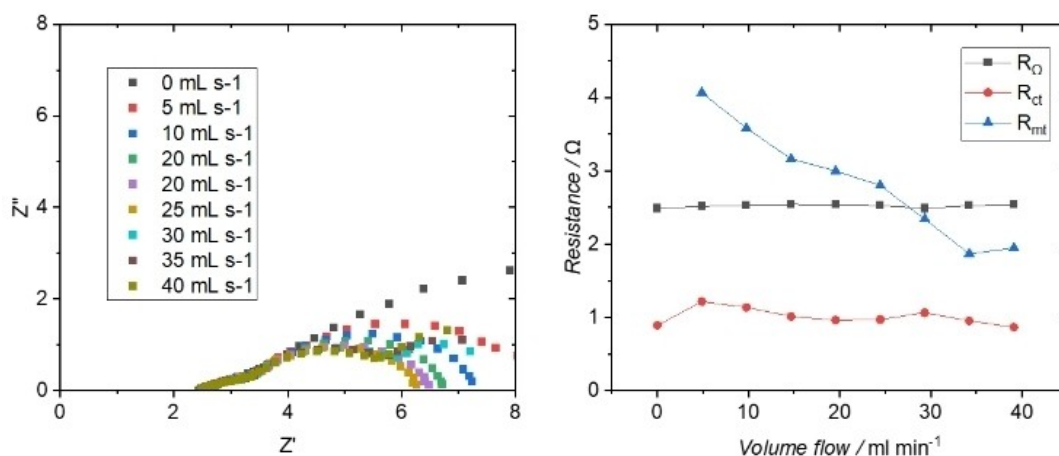
Batteries & Supercaps

Research Article
doi.org/10.1002/batt.202300045

**Chemistry
Europe**

European Chemical
Societies Publishing

Figure 5. Cyclic voltammogram of organic electrolyte (10 mM Fc and FcBF$_4$, 0.1 M TBABF$_4$, acetonitrile,) in flow RFB setup at different scan rates. The noise of the CV signal is caused by the additional, turbulentconvective mass transport during cycling.[38]

refreshing differences become more intense at higher electrochemical conversion rates, which can be seen in the increasing noise with increasing scan rate.[38] The impedance spectroscopy exhibits a low impedance (Figure 6), congruent with the multimeter reading of under 10 Ω (as explained in Figure 4). Higher flow rates result in a reduction of the mass transport resistance since the diffusion fraction of the material transport is reduced by increased convection. The charge transfer and cell resistance, on the other hand, remain almost constant over the entire flow rate range.

Battery performance

Though the potential of the RFB is negligible using the Fc/FcBF$_4$ or K$_4$[Fe^{II}(CN)$_6$]|K$_3$[Fe^{III}(CN)$_6$] redox pair, our purpose is to establish reproducible benchmark values using a well-known and stable redox-species.[35–37]

For aqueous systems, charging and discharging of the battery containing K$_4$[Fe^{II}(CN)$_6$]|K$_3$[Fe^{III}(CN)$_6$] at 2 C can be performed over 100 charge/discharge cycles with a Coulombic efficiency of >99% (Figure S9). Notably, higher C-rates lead to decomposition of the K$_3$[Fe^{III}(CN)$_6$], specifically, into Prussian blue over time, a process that is catalysed by protons in weak acidic medium.[39] Fluctuations of pH at electrode surfaces during cyclic voltammetry measurements are known to cause side reactions,[40] even in the presence of buffer.[41] In our case, although a potassium phosphate buffer was observed to retard the decomposition at higher C rates, discoloration still occurred at a lower rate, causing us to hold to the stable cycling at 2 C without the use of a buffer.

Potentiostatic cycling of for organic electrolyte was evaluated with the Fc/FcBF$_4$ redox couple, as proposed by Armstrong et al. (Figure 7).

In the first cycle, a Coulombic efficiency of 99.3% was achieved, decreasing to 88.9% over the course of 100 cycles (2.2 days). In addition, a charge efficiency of 87.8% and a discharge efficiency of 78.6% were achieved after 100 cycles. These measurements were performed at 2.08 mA cm^{-2}. The efficiency losses during the first 60 cycles can be attributed to the decomposition of the oxygen unstable FcBF$_4$ and residual oxygen in the setup, as also described by Armstrong et al. For the last 40 cycles the charge discharge profiles show good reversibility.

With the currently listed settings and conditions, the first RFB of the final design for aqueous measurements was run over 3000 h at 2000 pulses s^{-1} before the bearings got pushed out of alignment on account of wear of the motor head blocks, which could be helped by simply attaching a freshly printed motor head.

In between, the FEP tubing had to be replaced thrice because of minor cracks developing. The insertion point of the Teflon tubing had to occasionally be reinforced with more resin due to formation of salt at the opening, i.e., slow development of a leakage as a result of channel wear-down.

Figure 6. Impedance spectroscopy results of organic electrolyte (10 mM Fc and FcBF$_4$, acetonitrile, 0.1 M TBABF$_4$) in in-flow RFB setup at different flow rates (left) and more detailed resistance evaluation of cellular resistance (R_Ω), charge transfer resistance (R_{ct}) and mass transfer resistance (R_{mt}) (right).

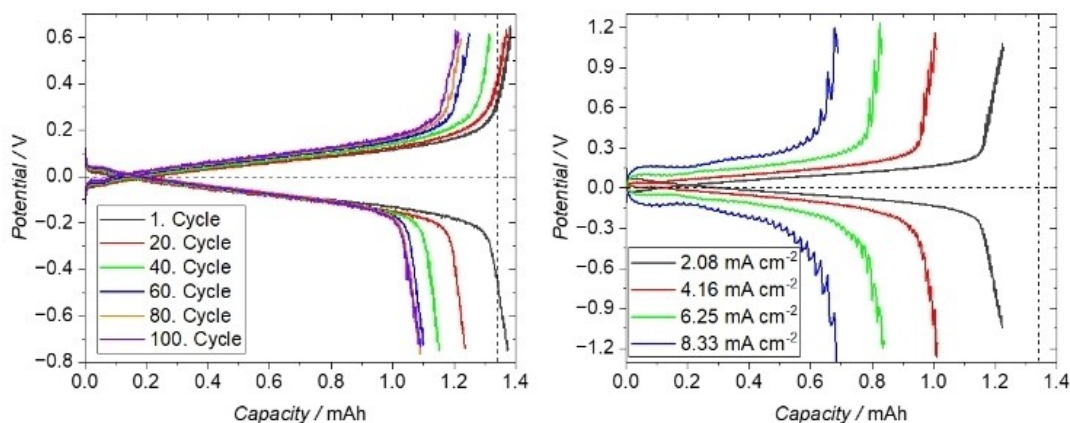**Batteries & Supercaps**

Research Article
doi.org/10.1002/batt.202300045

Chemistry Europe
European Chemical
Societies Publishing

Figure 7. (Left) Potential vs. capacity plots of 0.01 M Fc and $FcBF_4$ at 5 mA at a flow rate of 10 mL s^{-1} (5 mL in each respective electrolyte tank, applied currents 5 and -5 mA (2.08 mA cm^{-2}) every 20th cycle. (Right) Charge discharge cycling at different current densities.

The half-cells for organic redox-flow have shown no signs of breakdown as of 4000 h of operation, only requiring minor repairing and readjusting like replacing flow-through screws or readjusting the Teflon tube in the peristaltic pump. A detailed trouble-shooting list is provided in the Supporting information. Here, various experience-based optimizations and problem observations are described and explained. No further material fatigue or decomposition processes of the resin were observed over the course of several months.

Conclusions

In summary, we have shown that 3D-printing can be a valuable tool for creating inexpensive, readily accessible RFBs. The digital blueprint outlined in this contribution allows for any group with access to an (nowadays highly affordable) MSLA 3D-printer to create their own lab-scale RFBs including stepper motor and glove bag at about 230 € a piece. Of course, the modularity of 3D-printing does allow for upscaling as well as downscaling past the suggested scale, bearing in mind its effect on flow dynamics could alter results. Unlike commercial cells, the ease of modification of the 3D-printable flow cell, however, allows for complete flexibility to optimize for electrolyte-specific requirements (e.g., electrode size and material), although extensive verification was performed only at the current scale. Though ferrocene and $K_4[Fe^{II}(CN)_6]$ on their own are highly unsuitable as electrolyte for redox-flow, the measured data provide benchmark values for reproduction of aqueous and organic electrolyte systems. Ultimately, this digital blueprint significantly lowers the energetic and financial barrier for organic chemistry-oriented groups to contribute to creating the next generation battery.

Experimental Section

Materials

$K_3[Fe^{III}(CN)_6]$, $K_4[Fe^{II}(CN)_6]$ and KCl were purchased from TCI Chemicals and used as is. Fc, $FcBF_4$, $TBABF_4$ and anhydrous acetonitrile were purchased from Sigma Aldrich, where the conducting salt was dried under reduced pressure and 120 °C overnight and the acetonitrile was dried with molsieve. Fc and $FcBF_4$ were used as delivered. A detailed list of required materials for the RFB assembly and a corresponding cost analysis is shown in Table S1.

3D-printing

The resin used for this study was Liqcreate Composite-X for the RFB, which is chemically resistant to organic electrolytes and physically against pressure, cell and Prima Value Tough Resin for the peristaltic pump. 3D-printing at high resolution was done with a Phrozen Shuffle 4 K (XY-resolution 31 μm), as well as an Elegoo Mars 3 3D-printer (also 4 K, over a slightly larger building plate, XY-resolution 35 μm). Be aware that the printing components have to be aligned in such a way that no subsection gets printed in air during the layer-by-layer printing, i.e., best not orient screw channels or the current collector slot towards the build plate of the 3D-printer. Moreover, the half-cells should be printed on supports and in an angle (e.g., rotate 10 degrees in the X-direction and 20 degrees in the Y-direction). This ensures that the cell block can be taken off the build plate after printing, and that the bulk of the print is gradually supported instead of all at one go, risking that the supports break during printing. After completion, the channels of the cell block and screws were cleared with a needle to dispose of the higher viscosity (i.e., partially cured) resin residues, though it is also possible to adjust with a drill after further curing (Figure S11). After washing with isopropanol, the parts were further hardened by UV- and thermal curing steps. UV-curing was done with an Anycubic Wash & Cure 2.0 by irradiation with 405 nm for 1 h, with subsequent thermal curing in the oven overnight at 80 °C. Depending on the resin used, shrinkage may lead to a slight offset in screw versus cell threading, especially at lower effective resolution on, e.g., a Phrozen Transform (XY-resolution 67 μm). This can be easily fixed by refining the threads in the half-cells by using a thread cutter M6 drill attachment (or in absence thereof, using M6 metal screws more carefully) to adjust the half-cell head. The threading on the screws can be refined by repeatedly screwing and

unscrewing a metal bolt. If the bolt does not fit over, use sandpaper to file down part of the initial threading. Once the bolt is over the threading it should fairly smoothly continue over the rest of the thread.

Electrolyte solution

For the purpose of setting a consistent benchmark, $K_4[Fe^{II}(CN)_6] | K_3[Fe^{III}(CN)_6]$ was selected as a redox-pair for aqueous battery cycling performance evaluation.[36,37] Electrolyte solutions were formulated with 1 M KCl as supporting electrolyte, containing 0.05 M $K_4[Fe^{II}(CN)_6]$ for the anolyte and 0.05 M $K_3[Fe^{III}(CN)_6]$ for the catholyte compartment. The 3 mL Eppendorf® tubes used in this study as electrolyte tanks were filled with a volume of 2 mL electrolyte solution each, and stuck in upside-down small septa that served to establish traction and balance. Alternatively, glass vials can be used as well. Either way, a pair of 2.5 mm holes were drilled into each of the caps to lead the tubing through.

As organic electrolyte benchmark the ferrocene | ferrocene tetra-fluoroborate redox pair was selected, as shown by Armstrong et al.[35] Therefore, 0.01 M of the active material and 0.1 M TBABF$_4$ as a supporting electrolyte were dissolved in acetonitrile in an argon filled glove box. 5 mL of the electrolyte was added into 20 mL glass vials, which served as tanks. The vials were sealed and transferred to the nitrogen filled glove bag along with another pair of plastic caps with 2.5 mm holes drilled into them to be able to ultimately lead the tubing through. Further cell assembly was done in the nitrogen filled glove bag.

Cell preparation for assembly

Prior to assembling the cell, confirm the fit of the screws to the cell thread, making adjustments by using a thread cutter for the cell threads, or screwing and unscrewing the appropriate bolt to the printed screws. Graphite blocks can be cut to size with a (small) sawblade to fit into the 1.0 by 2.4 cm respective slots in each half-cell, making use of sandpaper or files to make the final, finer adjustments to the slot and graphite block, ultimately tapping the latter into the slot by using a hammer. It is important to not have too tight of a fit - if the graphite block hardly goes in, forcing it in with a hammer will split open the cell. After insertion, adjust the topside of the graphite block by chafing off a groove (i.e., like a gutter, ca. 2.5 mm deep in the middle, see Figure S5A), serving to counter too tight of a compression of the carbon felt, which would lead to a drop-in flow rate and efficiency. Here, the groove should be deep enough to fit the carbon felt almost completely in, in order to reduce inner cell pressure and thereby prevent leakages. If the flow rate happens to be subpar, either this or the clogging of tubing/channels will be the most likely cause. A hammer can be used to completely insert the graphite block. Take caution that there is not too much resistance during insertion, since this will only exert stress on the half-cell, in extreme cases causing it to split while forcing the graphite block in. Conversely, a loose fit can be easily adjusted by dripping in resin to the sides, with further hardening through UV-curing and heating to 80 °C over at least one night. Next, drill through the working and counter electrode insertion points to the side of the cell with a 2 mm drill bit (see Figure 3), drilling roughly 2 mm into the graphite, serving to increase the contact of the titanium rod that will be wedged in instead of it having a minute interfacial contact (once graphite dust comes out after drilling, it should be sufficient). Note that bad contact and thus high resistance can still lead to a measurable change in current in cyclic voltammetry, a flat retracing line being indicative of this (Figure S14). Drill through any of the available insertion points for the reference electrode in case of one of the

two half-cells, continuing all the way through the graphite block in order to enable contact of the reference electrode with the electrolyte solution. The hole should be at least 2 mm to really ensure good electrolyte contact. Cut off two pieces of titanium rod, each 4 to 5 cm, and insert them ≈1 cm through a corresponding screw. Using Teflon tape around the screws initially, screw until a significant resistance is met, and then hammer the titanium rod in further to create good contact with the graphite block. First assess that the resistance is approximately under 10 Ω between the graphite block and the titanium rod, and then measure the impedance of an aqueous KCl solution in a full cell (see **Assembly/disassembly of the half-cells** Section below) to observe if it follows the same trend as Figure 6. If so, add (wet) resin to the screw thread as well as the titanium rod insertion and exertion points, and UV- and thermally cure in the screw (irradiate several minutes from various angles, and cure in an 80 °C oven over at least one night) to ensure a leak-tight seal. A resistance of 10 Ω should still be measurable between the graphite block and the titanium rod, and the impedance spectrum should exhibit the same pattern as before.

For the RE, a leakless electrode can be inserted into the corresponding screw, as described above, with the help of a silicon sealing rubber, Teflon tape or resin, also as described above. Alternatively, a permanent Ag | AgCl electrode can be made by inserting a Ag | AgCl wire through a screw with a small (potentially drilled) channel, using resin to completely seal the inner channel with subsequent UV- and thermal curing (Figure S6). The Ag | AgCl wire can be made by holding a 5 cm silver wire against platinum in a 1 M aqueous KCl solution at 9 V for approximately 30 seconds, until the appearance becomes a dull grey. At first, i.e., while running initial tests on the cell, the reference electrode is best inserted with Teflon tape, making sure that the measurements run as desired before permanently curing the screw into the block as described for the titanium rods. For guaranteeing a correct reference potential, a self-made RE should be checked with a saturated calomel electrode or ferrocene as a reference standard beforehand. Afterwards, the measured RE potential can be adjusted accordingly to match SCE or ferrocene values.

Assembly/disassembly of the half-cells

The large O-rings are placed in their slots around the graphite block in both cells. Four compression screws are inserted into the anolyte half-cell (i.e., without a reference electrode sticking out, this half-cell can lay flat on that side) with the graphite block facing up (Figure S5A). The footing should be stable, leaning on the 4 screw heads. Two 1.0 by 2.4 cm carbon felt sheets are cut and the 4 corners of each are rounded by cutting off ca 1 mm, and one is placed on top of the graphite into the gutter. An area in two silicone rubbers is cut out corresponding to the 1.0 by 2.4 cm electrode area as well as the semi-circular flow area at each 1.0 cm end, and openings are stamped/cut out for the compression screws in each of the four corners. The silicone rubber is guided onto the half-cell over the screws (Figure S5B). A cut-to-size membrane or separator (in our case Nafion® N551Na for aqueous cell testing and a Celgard® 2500 for organic) that covers an area exceeding that of the large O-ring, but just short of the screws, is placed. The corners of the membrane can be cut off to ease the fitting, it does not have to have a perfect size. As a reminder, many membranes have a protective layer against drying out, which has to be removed before use (Figure S5C). If a reinforced membrane is used, which is usually thicker, Teflon tape should be folded around all sides, to hinder electrolyte slowly leaking out laterally through the membrane (Figure S13, right). The second silicone rubbers is guided over the membrane or separator, followed by placing the second

Batteries & Supercaps

Research Article
doi.org/10.1002/batt.202300045

Chemistry
Europe
European Chemical
Societies Publishing

carbon felt in the middle. The second half-cell is guided over the screws until it compresses the just-formed sandwich. The screws are gradually tightening each one by one over and over with the corresponding bolts on the complete opposite side of the cell sandwich (i.e., where the reference electrode screw is sticking out of the cell), until they do not give in to moderate to tight force anymore (Figure S5D). CAUTION: during tightening the chances are biggest that the cell slips off and a screw breaks off. Disassembly is done in reverse order, taking care that the membrane is not exposed to air for too long to avoid drying out, in case the membrane is not reinforced.

Stepper motor and stepper motor control

Standard silicon tubing (ID 1.5 mm, OD 2.5 mm) or PharMed® BPT from VWR (ID 1.52 mm, OD 3.22 mm) can be led through and pinned down in the pump block as shown in Figure 1, one end of each leading to a half-cell, and the other leading to their respective electrolyte tank. The pair of screws on the other end of the half-cell is directly connected with silicon tubing to each respective electrolyte tank.

The stepper motors are controlled by the free of charge Pololu® Tic control software (Figure S3). Under motor settings, step mode was set to $\frac{1}{4}$ step, with a current limit of 640 mA and decay mode at fast. Here, the maximum speed can also be adjusted beyond the standard setting, for which 8000.0000 pulses/s suffices.

Potentiostatic measurements

An Autolab® Multipotentiostat was used in this study, controlled by Nova 2.1 software. (see Figure S10) Working and counter electrode were carbon felt-topped graphite blocks, and the reference electrode either a leakless electrode or an Ag|AgCl wire, all as according to Figure 4. Unless otherwise stated, cyclic voltammograms were recorded at a scan rate of 1 mV s^{-1}. Impedance spectra were acquired with a frequency range of 0.1 to 10^6 Hz with an amplitude of 10^{-5} A$_{RMS}$. Charge/discharge cycling was performed by applying 5 mA and -5 mA, respectively, with cut-off potentials at 0 and 0.325 V and 0.6 and -0.7 V for aqueous and organic electrolytes, respectively.

Acknowledgements

Conflict of Interest

The authors declare no conflict of interest.

Data Availability Statement

The data that support the findings of this study are available in the supplementary material of this article.

[1] a) S. Dühnen, J. Betz, M. Kolek, R. Schmuch, M. Winter, T. Placke, *Small Methods* **2020**, *4*, 2000039; b) X. Li, S. Wang, *CSEE J. Energy Syst.* **2019**, *5*, 1026–1040.

[2] a) M. L. Perry, K. E. Rodby, F. R. Brushett, *ACS Energy Lett.* **2022**, *7*, 659; b) E. Sánchez-Díez, E. Ventosa, M. Guarnieri, A. Trovò, C. Flox, R. Marcilla, F. Soavi, P. Mazur, E. Aranzabe, R. Ferret, *J. Power Sources* **2021**, *481*, 228804.

[3] J. Noack, N. Roznyatovskaya, T. Herr, P. Fischer, *Angew. Chem. Int. Ed. Engl.* **2015**, *54*, 9776–9809.

[4] P. Leung, A. A. Shah, L. Sanz, C. Flox, J. R. Morante, Q. Xu, M. R. Mohamed, C. Ponce de León, F. C. Walsh, *J. Power Sources* **2017**, *360*, 243–283.

[5] J. Cao, J. Tian, J. Xu, Y. Wang, *Energy Fuels* **2020**, *34*, 13384–13411.

[6] a) J. Luo, B. Hu, M. Hu, Y. Zhao, T. L. Liu, *ACS Energy Lett.* **2019**, *4*, 2220–2240; b) V. Viswanathan, A. Crawford, D. Stephenson, S. Kim, W. Wang, B. Li, G. Coffey, E. Thomsen, G. Graff, P. Balducci, *J. Power Sources* **2014**, *247*, 1040–1051; c) C. Minke, T. Turek, *J. Power Sources* **2018**, *376*, 66–81.

[7] T. D. Ngo, A. Kashani, G. Imbalzano, K. T. Nguyen, D. Hui, *Composites Part B* **2018**, *143*, 172–196.

[8] P. Leung, X. Li, C. Ponce de León, L. Berlouis, C. T. J. Low, F. C. Walsh, *RSC Adv.* **2012**, *2*, 10125–10156.

[9] S. C. Ligon, R. Liska, J. Stampfl, M. Gurr, R. Mülhaupt, *Chem. Rev.* **2017**, *117*, 10212–10290.

[10] M. R. Behrens, H. C. Fuller, E. R. Swist, J. Wu, M. M. Islam, Z. Long, W. C. Ruder, R. Steward, *Sci. Rep.* **2020**, *10*, 1543.

[11] T. Ching, J. Vasudevan, H. Y. Tan, C. T. Lim, J. Fernandez, Y.-C. Toh, M. Hashimoto, *HardwareX* **2021**, *10*, e00202.

[12] V. Sans, *Curr. Opin. Green Sustain. Chem.* **2020**, *25*, 100367.

[13] a) H. Sun, H. Takahashi, N. Nishiumi, Y. Kamada, K. Sato, K. Nedu, Y. Matsushima, A. Khosla, M. Kawakami, H. Furukawa, *J. Electrochem. Soc.* **2019**, *166*, B3125-B3130; b) A. Ambrosi, R. D. Webster, *Curr. Opin. Electrochem.* **2020**, *20*, 28–35.

[14] L. F. Arenas, F. C. Walsh, C. P. de León, *ECS J. Solid State Sci. Technol.* **2015**, *4*, P3080-P3085.

[15] Z. Lyu, G. J. Lim, J. J. Koh, Y. Li, Y. Ma, J. Ding, J. Wang, Z. Hu, J. Wang, W. Chen, *Joule* **2021**, *5*, 89–114.

[16] M. P. Browne, E. Redondo, M. Pumera, *Chem. Rev.* **2020**, *120*, 2783–2810.

[17] a) M. P. Down, E. Martínez-Periñán, C. W. Foster, E. Lorenzo, G. C. Smith, C. E. Banks, *Adv. Energy Mater.* **2019**, *9*, 1803019; b) D. D. Gu, W. Meiners, K. Wissenbach, R. Poprawe, *Inter. Mater. Rev.* **2012**, *57*, 133–164; c) N. Kaishubayeva, C. Ponce de León, F. C. Walsh, L. F. Arenas, *J. Chem. Technol. Biotechnol.* **2021**, *96*, 1818–1831; d) M. J. Whittingham, R. D. Crapnell, C. E. Banks, *Anal. Chem.* **2022**, *94*, 13540–13548.

[18] F. C. Walsh, L. F. Arenas, C. Ponce de León, *Trans. IMF* **2020**, *98*, 65–72.

[19] L. F. Arenas, C. Ponce de León, F. C. Walsh, *J. Electrochem. Soc.* **2020**, *167*, 23504.

[20] H. O'Connor, J. J. Bailey, O. M. Istrate, P. A. A. Klusener, R. Watson, S. Glover, F. Iacoviello, D. J. L. Brett, P. R. Shearing, P. Nockemann, *Sustain. Energy Fuels* **2022**, *6*, 1529–1540.

[21] K. Amini, M. D. Pritzker, *J. Power Sources* **2021**, *506*, 230237.

[22] M. J. Watt-Smith, P. Ridley, R. Wills, A. A. Shah, F. C. Walsh, *J. Chem. Technol. Biotechnol.* **2013**, *88*, 126–138.

[23] C. Ponce de León, A. Frías-Ferrer, J. González-García, D. A. Szánto, F. C. Walsh, *J. Power Sources* **2006**, *160*, 716–732.

[24] L. F. Arenas, C. Ponce de León, F. C. Walsh, *Curr. Opin. Electrochem.* **2019**, *16*, 117–126.

[25] E. Knudsen, P. Albertus, K. T. Cho, A. Z. Weber, A. Kojic, *J. Power Sources* **2015**, *299*, 617–628.

[26] Liu, Z, Jiang, Q, Zhang, Y, Li, T, & Zhang, H. "Sustainability of 3D Printing: A Critical Review and Recommendations." Proceedings of the ASME 2016 11th International Manufacturing Science and Engineering Conference. Volume 2: Materials; Biomanufacturing; Properties, Applications and Systems; Sustainable Manufacturing. Blacksburg, Virginia, USA. June 27–July 1, **2016**.

[27] Thingiverse.com, "Precise Peristaltic Pump by iGEM Aachen", can be found under https://www.thingiverse.com/thing:2619479, **2023**.

[28] "Pololu - 3.1. Installing Windows drivers and software", can be found under https://www.pololu.com/docs/0 J71/3.1, **2023**.

Batteries & Supercaps

Research Article
doi.org/10.1002/batt.202300045

Chemistry Europe
European Chemical
Societies Publishing

[29] P. K. Leung, C. Ponce de León, F. C. Walsh, *Electrochem. Commun.* **2011**, *13*, 770–773.

[30] a) X. Ke, J. M. Prahl, J. I. D. Alexander, J. S. Wainright, T. A. Zawodzinski, R. F. Savinell, *Chem. Soc. Rev.* **2018**, *47*, 8721–8743; b) F. C. Walsh, L. F. Arenas, C. Ponce de León, *Curr. Opin. Electrochem.* **2019**, *16*, 10–18.

[31] L. F. Arenas, C. Ponce de León, F. C. Walsh, *J. Energy Storage* **2017**, *11*, 119–153.

[32] C. A. Machado, G. O. Brown, R. Yang, T. E. Hopkins, J. G. Pribyl, T. H. Epps, *ACS Energy Lett.* **2021**, *6*, 158–176.

[33] M. H. Chakrabarti, N. P. Brandon, S. A. Hajimolana, F. Tariq, V. Yufit, M. A. Hashim, M. A. Hussain, C. Low, P. V. Aravind, *J. Power Sources* **2014**, *253*, 150–166.

[34] F. C. Walsh, C. Ponce de León, *Electrochim. Acta* **2018**, *280*, 121–148.

[35] C. G. Armstrong, R. W. Hogue, K. E. Toghill, *J. Electroanal. Chem.* **2020**, *872*, 114241.

[36] W. Lee, A. Permatasari, Y. Kwon, *J. Mater. Chem. C* **2020**, *8*, 5727–5731.

[37] Y. Chen, M. Zhou, Y. Xia, X. Wang, Y. Liu, Y. Yao, H. Zhang, Y. Li, S. Lu, W. Qin, *Joule* **2019**, *3*, 2255–2267.

[38] L. Kortekaas, S. Fricke, A. Korshunov, I. Cekic-Laskovic, M. Winter, M. Grünebaum, *Batteries* **2023**, *9*, 4.

[39] R. Yang, Z. Qian, J. Deng, *J. Electrochem. Soc.* **1998**, *145*, 2231.

[40] a) P. Bollella, A. Melman, E. Katz, *ChemElectroChem* **2020**, *7*, 3386–3403; b) I. Katsounaros, J. C. Meier, S. O. Klemm, A. A. Topalov, P. U. Biedermann, M. Auinger, K. J. Mayrhofer, *Electrochem. Commun.* **2011**, *13*, 634–637.

[41] J. Wang, H. Wang, S. Guo, X. Jia, Y. Zhong, Y. Han, M. Lin, S. Wang, F. Zhao, J. Fu, *J. Electrochem. Soc.* **2014**, *161*, H443-H446.